

Original Article

Cite this article: Bansal U, Banerjee S, Pande K, and Ruidas DK (2020) Unusual seawater composition of the Late Cretaceous Tethys imprinted in glauconite of Narmada basin, central India. *Geological Magazine* **157**: 233–247. <https://doi.org/10.1017/S0016756819000621>

Received: 4 March 2019

Revised: 3 May 2019

Accepted: 13 May 2019

First published online: 2 July 2019


Keywords:

glauconite; shallow marine; Late Cretaceous; Bagh Group; Palaeo-Tethys; Ce anomaly; sub-oxic diagenesis

Author for correspondence:

Santanu Banerjee, Email: santanu@iitb.ac.in

Unusual seawater composition of the Late Cretaceous Tethys imprinted in glauconite of Narmada basin, central India

Udita Bansal^{1,2}, Santanu Banerjee² , Kanchan Pande² and Dhiren K. Ruidas²

¹Department of Earth Sciences, Indian Institute of Technology Roorkee, Roorkee 247667, Uttarakhand, India and

²Department of Earth Sciences, Indian Institute of Technology Bombay, Powai, Mumbai 400076, India

Abstract

A detailed investigation of a glauconite bed within the Late Cretaceous Bryozoa Limestone Formation of the Bagh Group in central India, as well as the study of existing records, reveals the existence of a 'glauconitic sea' along the margins of the Palaeo-Tethys Ocean during the Late Cretaceous Epoch. The authigenic green mineral formed abundantly on shallow seafloors unlike in its modern, deep-sea counterpart. We present an integrated petrographical, geochemical and mineralogical investigation of the glauconite within Late Cretaceous transgressive deposits to highlight its unique geochemistry with moderate Fe₂O₃ and high Al₂O₃, SiO₂, MgO as well as K₂O contents. X-ray diffractogram parameters identify the 'evolved to high evolved' nature of the glauconite while Mössbauer spectroscopic study reveals the dominance of Fe³⁺ compared to Fe²⁺ in the atomic structure. The rare earth elements (REE) pattern of glauconite reveals moderate light-REE/heavy-REE (LREE/HREE) fractionation and weak negative Eu anomaly. The Ce anomaly of the glauconite indicates a sub-oxic diagenetic condition. We propose that Late Cretaceous glauconites formed within a shallow marine depositional setting across the Tethyan belt because of enhanced supply of K, Si, Al, Fe, Mg cations through continental weathering under the extant greenhouse climate.

1. Introduction

Glauconite is an excellent marker of stratigraphic condensation associated with transgressive deposits (Amorosi, 1995, 1997, 2011; Amorosi & Centineo, 1997; Banerjee *et al.* 2012a, b, 2015, 2016a, b; Bansal *et al.* 2017, 2018). A recent review indicates unusually high abundance of glauconite during the Early Cretaceous, Late Cretaceous and Eocene, accounting for roughly 11 %, 18 % and 12 % of a total record of 453 glauconite occurrences respectively (Banerjee *et al.* 2016b). As global sea level rise inundated almost all the continents during the Cretaceous, extensive glauconite formed in marine transgressive deposits (Odin *et al.* 1977; Glenn & Arthur, 1990; Henderson, 1998; Mishra & Sen, 2001; Baioumy, 2007; Rifai & Shaaban, 2007; Martinec *et al.* 2010; Tewari *et al.* 2010; Zalat *et al.* 2012; Banning *et al.* 2013; Anan, 2014). Extensive epeiric seas dominated the Cretaceous, forming wide carbonate platforms with deposition of abundant organic-rich dark-coloured mud in deep seas and on continental shelves.

While the authigenic glauconite in recent times forms preferably within outer shelf and slope environments (Odin & Matter, 1981; Amorosi, 1997, 2012; Banerjee *et al.* 2016b), the Late Cretaceous variety is reported from shallow marine environment (Banerjee *et al.* 2016b). The exact reasons for the different palaeobathymetric implications of glauconites formed at different times are not yet understood. Chafetz & Reid (2000) proposed an unusual seawater composition for shallow marine glauconitization in Palaeozoic seas. We investigate the factors behind the formation of Late Cretaceous glauconite and intend to assess the palaeo-redox conditions and seawater composition. Glauconite occurs within the Coniacian platform carbonate succession of the Narmada basin in central India. Detailed petrography reveals mode of occurrence of the glauconite, while rare earth elements (REE) data unravel palaeo-depositional conditions. Finally, factors facilitating the extensive formation of glauconite across the margins of palaeo-Tethys are explored.

2. Geological background

The Late Cretaceous Bagh Group in central India represents deposition within the eastwardly transgressing arm of Tethys and crops out in the western part of the ~1200 km long Narmada basin (Tandon, 2000; Fig. 1). The three-tiered Bagh Group is a mixed siliciclastic-carbonate succession comprising Nimar, Nodular Limestone and Bryozoa Limestone formations from the bottom to the top (Gangopadhyay & Maiti, 2012; Figs 2 and 3a), the age of which was originally assigned as Turonian-Coniacian on the basis of the ammonoid Placenticeratids (Chiplonkar &

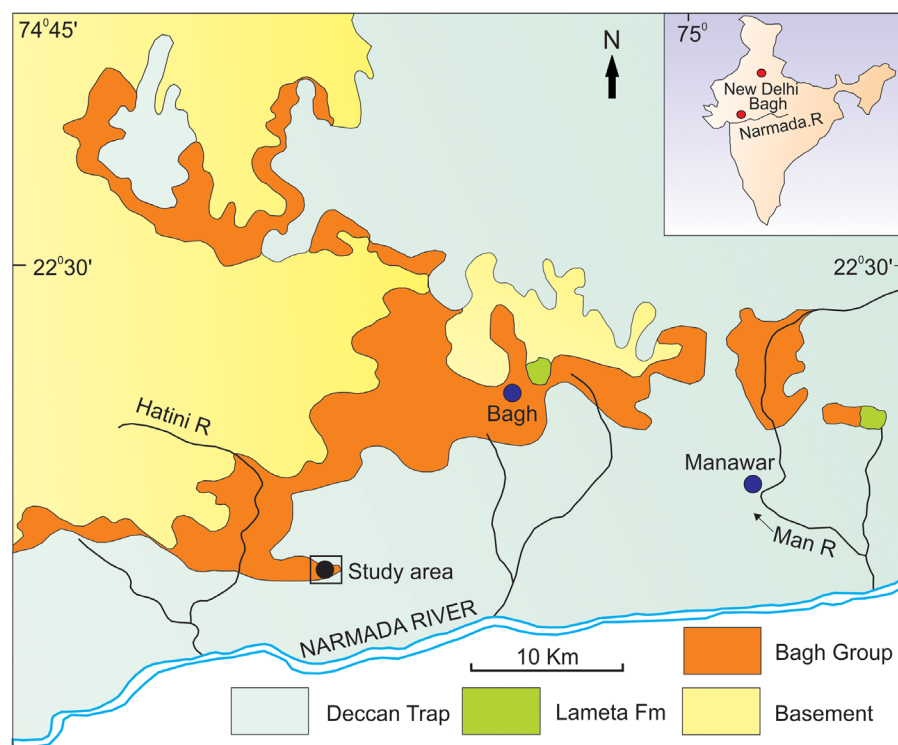


Fig. 1. (Colour online) Geological map of western Narmada basin showing distribution of Deccan trap, Bagh Group of rocks and basement of Cretaceous age. The study area is marked in black rectangle.

Ghare, 1976). Recent biostratigraphic investigation constrains Cenomanian, Turonian and Coniacian ages for the Nimar, Nodular Limestone and Bryozoan Limestone formations respectively (Kumar *et al.* 2018).

Resting directly on the Precambrian basement, the Nimar Formation (~30 m thick) consists of a shallow marine siliciclastic succession (Bose & Das, 1986). The overlying ~6.5 m thick Nodular Limestone Formation comprises three non-repetitive facies, viz. wackestone–mudstone alternations, nodular wackestone and poorly bedded wackestone in ascending order in the study area around Ratitalai (Fig. 2). The overlying ~3.5 m thick Bryozoan Limestone begins with a cross-stratified rudstone consisting predominantly of broken shells of bryozoans, bivalves, gastropods, brachiopods and echinoids. It consists of three facies, viz. cross-stratified rudstone, planar laminated rudstone and faintly laminated packstone. The planar laminated rudstone at the top, hosting the glauconite, contains abundant clastics, including, quartz, feldspars and mud fragments (Fig. 2).

The 40–60 cm thick glauconitic bed within the Bryozoan Limestone Formation occurs in the top part of the transgressive deposit of the Bagh Group. It gradationally passes upward to the overall prograding Lameta Formation as content of siliciclastics increases significantly (Tandon, 2000; Bansal *et al.* 2018). The dominance of fine-grained sedimentary rocks, intact nature of the bioclasts and the facies association of the Nodular Limestone Formation indicate a shallow marine restricted platform–tidal flat system (Gangopadhyay & Maiti, 2012; Ruidas *et al.* 2018). Moderate sorting of bioclasts, abundance of current structures, local reactivation surfaces and bipolarity of current structures suggest deposition in tidal channels.

3. Materials and methods

This study includes samples collected from the outcrops of the Ratitalai Section of the Bagh Group. Precise sample positions

are marked in the graphic log (Fig. 2). Detailed petrography was carried out using a Leica DM 4500P polarizing microscope connected to a Leica DFC420 camera. All rock samples were powdered and processed to obtain glauconite pellets. Processing of samples included wetting of the samples and treatment with anhydrous Na_2CO_3 powder and H_2O_2 solution before heating for 15–20 min on a hot plate. The treated samples were finally cooled, washed and oven-dried for 24 hours. Clean glauconite pellets were further picked for geochemical and mineralogical analysis using a Zeiss Stemi 2000 stereo zoom microscope. About 0.1 g of glauconite pellets was powdered and ultra-sonicated for preparation of smear mounts. These smear mounts were scanned from 1° to 70° (step size $0.026^\circ/2\theta$), using nickel filter copper radiation at a scan speed of 96 s/step in an Empyrean X-Ray Diffractometer with Pixel 3D detector at the Department of Earth Sciences, Indian Institute of Technology Bombay. The glauconite pellets were examined under three different modes of scanning, viz., air-dried, after ethylene glycol treatment and after heating at 400°C , for 2 hours maintaining the same instrumental settings. Major element concentrations in glauconite were examined in five thin sections on 34 points using a Cameca SX 5 Electron Probe Micro Analyzer at the Department of Earth Sciences, Indian Institute of Technology Bombay, with accelerating voltage 15 kV, specimen current of 40 nA and beam diameter of $1\ \mu\text{m}$ (peak 10–20 s and background counting 5–10 s) with analytical error of less than 1%. Standards included minerals as well as synthetic phases. Concentrations of REE were determined using a Thermo Fisher Scientific, Germany (Element XR) instrument at the Thermo Fisher Lab in Mumbai. About 25 mg of cleaned glauconite pellets was precisely weighed and dissolved in a mixture of ~2.5 mL of HF-HNO_3 (2:1) in Teflon bombs for REE analysis. The solution was kept in an ultrasonic bath for 45 min, evaporated and dried down. The residue was treated with concentrated 8N HNO_3 and evaporated. The same step was repeated three times before diluting the sample with 25 mL of 1N HNO_3 . Ruthenium (Ru) was added as internal standard to

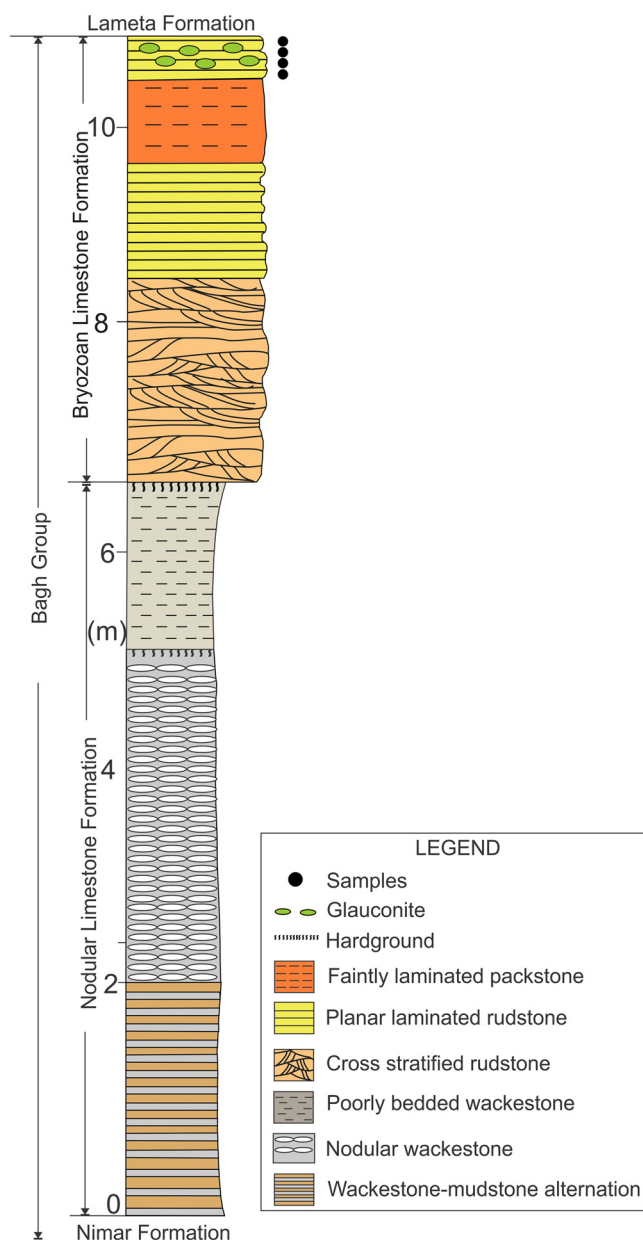


Fig. 2. (Colour online) Lithostratigraphic framework of the Bagh Group (note occurrence of glauconite near the top, sample position marked by solid circles).

all samples and standards to monitor the instrumental drift induced during analysis. US Geological Survey (USGS) geochemical reference standards (SCO-1, SCO-2, SBC-1) were used to assess the accuracy of the analyses.

4. Results

4.a. Sedimentological background

The Nodular Limestone Formation comprises three non-repetitive facies, viz. wackestone–mudstone alterations, nodular wackestone and poorly bedded wackestone in ascending order in the study area around Ratitalai (Fig. 2). All three facies of the Nodular Limestone formation are almost devoid of primary sedimentary structures. Juvenile tests of echinoderms, molluscs and gastropods sporadically occur within the constituent facies. The basal ~2 m thick

wackestone–mudstone facies exhibits alternations between planar and wavy bedded wackestone and mudstone (Fig. 3b). Wackestone beds are tabular, irregular and knobby, often exhibiting diffused planar laminae. Bed thickness varies from 3 to 7 cm. Both mudstone and wackestone beds exhibit desiccation cracks. The overlying 3.5–5 m thick, nodular wackestone facies is characterized by the conspicuous nodularity (Fig. 3b). The average diameter of nodules is ~5 cm. Desiccation cracks are common within the facies. Highly impregnated Fe-oxide borings and localized *Thalassinoides* burrows mark the top of the facies. The uppermost facies of the Nodular Limestone Formation consist dominantly of wackestone with thin mudstone interbeds. The thickness of the facies varies from 3.5 to 4 m in the study area. A 20 cm thick hardground with highly impregnated Fe-oxide borings occurs at the top. *In situ* root traces are frequent.

The Bryozoan Limestone Formation consists of three facies: cross-stratified rudstone, planar laminated rudstone and faintly laminated packstone. The cross-stratified rudstone facies consists of reddish to greyish brown, 30–90 cm thick tabular cross-beds of rudstones (Fig. 3c). It consists entirely of reworked bioclasts including bryozoans, bivalves, gastropods, brachiopods and echinoids. Reactivation surfaces occur within cross-stratified sets locally. *Thalassinoides* burrows are uncommonly present. The overlying glauconitic, planar laminated rudstone facies varies in thickness from 40 cm to 1 m and alternates with a faintly laminated packstone (Figs 2 and 3d). The content of siliciclastics is significantly high within the planar laminated rudstone (avg. ~50 %) compared to the background facies. The siliciclastics include quartz, feldspars and mud fragments, while allochems consists of broken bioclasts of bryozoans, bivalves, gastropods and echinoid spines. The occurrence of abundant oysters marks the top of the facies. The thickness of the faintly laminated packstone, sandwiched between two planar laminated rudstone beds, ranges from 1 to 1.7 m. Glauconite occurs within the top 20 cm thick rudstone overlying this packstone.

The underlying Nimar Formation consists predominantly of shallow marine sandstones (Bose & Das, 1986; Ahmad & Akhtar, 1990; Akhtar & Ahmad, 1991; Bhattacharya & Jha, 2014). Curtailment of clastic supply at the end of deposition of the Nimar Sandstone facilitated the deposition of carbonate sediments. The dominance of fine-grained sediments, thin and very small shells and intact nature of the bioclasts indicate a low-energy depositional setting for the Nodular Limestone Formation. Recent petrographic investigations reveal a wide spectrum of emergence features within the constituent facies of the Nodular Limestone Formation including rhizoconcretions, alveolar texture, *in situ* brecciation and micro-nodulation (Ruidas, Paul & Gangopadhyay, 2018). The facies association of the Nodular Limestone indicates a shallow marine restricted platform–tidal flat system with periodic subaerial exposure (Ruidas *et al.* 2018). The peritidal nature of the Nodular Limestone Formation is also indicated in previous studies (Gangopadhyay & Halder, 1996; Akhtar & Khan, 1997; Gangopadhyay & Bardhan, 2000; Jaitly & Ajane, 2013; Ruidas *et al.* 2018). The Bryozoan Limestone Formation begins with a cross-stratified rudstone in most places. Moderate sorting of bioclasts, rarity of mud and abundance of current structures indicate a high-energy depositional environment. The occurrence of reactivation surfaces and bipolarity of current structures suggests deposition in tidal channels. Planar laminae as well as abundant siliciclastics indicate a shallow marine, high-energy depositional condition.

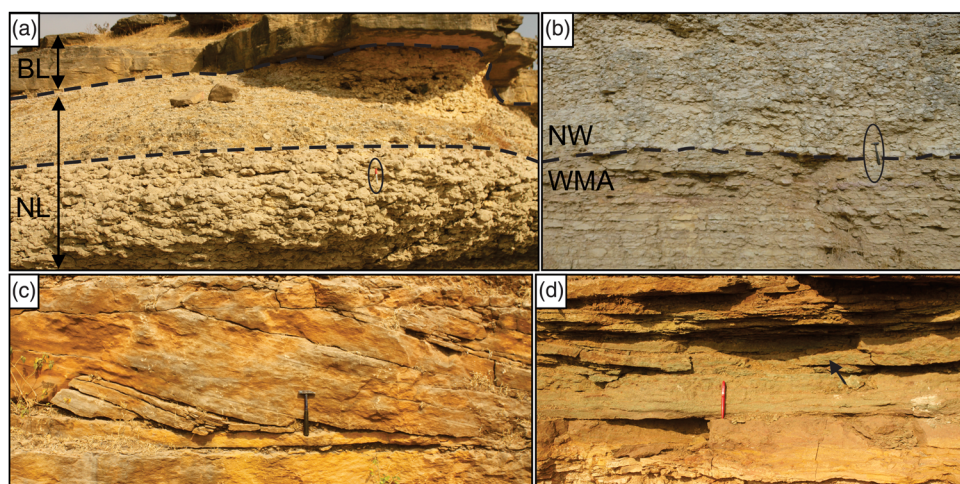


Fig. 3. (Colour online) Field photographs showing (a) the contact between Nodular Limestone and Bryozoan Limestone formations, (b) the contact between wackestone-mudstone alteration (WMA) and nodular wackestone (NW) facies of Nodular Limestone Formation, (c) cross-stratified rudstone facies and (d) planar laminated rudstone facies containing glauconite bed marked by arrow (hammer length 38 cm; coin diameter 2.5 cm; pen length 14 cm).

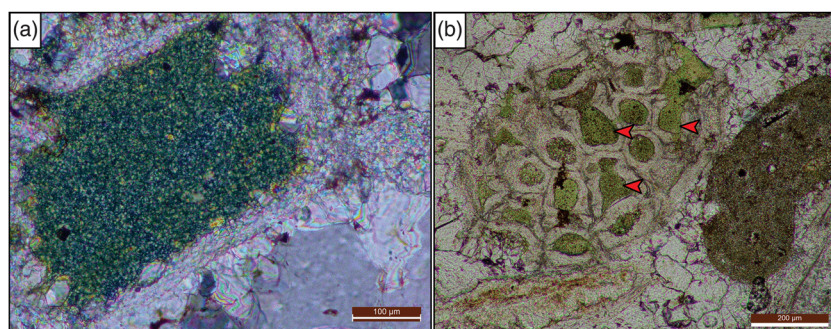


Fig. 4. (Colour online) Photomicrographs (a) under cross polars showing glauconitized feldspar; (b) glauconite infillings within bryozoan test marked by red arrows.

The Nodular Limestone Formation is overall deepening upward and it represents the upper part of a transgressive deposit. The lower part of the same transgressive deposit incorporates the Nimar Formation (Bose & Das, 1986). The glauconite bed within the Bryozoan Limestone Formation, therefore, occurs near the top part of a shallow marine transgressive deposit. It gradationally passes upward to the overall prograding Lameta Formation with increase in the content of siliciclastics.

4.b. Petrography of glauconite

Glauconite grains constitute up to ~30 % of the rock by volume within the planar laminated rudstone facies at the top of the Bryozoan Limestone Formation. Glauconite occurs as two different forms: as replacement of K-feldspars, referred to as glauconitized feldspars (Fig. 4a), and as infillings within pores, and carapaces of bioclasts, referred to here as glauconite infillings (Fig. 4b). The glauconite replaces K-feldspar along cleavages and fractures, forming linear and interconnected stringers which are up to 150 μm long. The K-feldspar is thoroughly altered to glauconite in places, leaving no trace of the primary mineral (Fig. 4a). On the other hand, glauconite infillings occur within zoecia of bryozoa (Fig. 4b), pores of echinoid and carapaces of ostracoda. The average diameter of individual bryozoan infillings varies between 40 and 250 μm . Both varieties of glauconite exhibit light green to olive green colour in plane polarized light and high-interference colour under crossed polars. The absence of broken pellets as well as poor sorting of glauconite grains suggest an autochthonous nature for the glauconites (Amorosi, 1995, 1997; Hesselbo & Huggett, 2001; Longuépée & Cousineau, 2006; Banerjee *et al.* 2012a, b, 2015, 2016a).

4.c. Mineralogical characteristics of glauconite

The air-dried samples of glauconite pellets exhibit a prominent basal reflection (001) at 10.04 \AA , and relatively weaker reflections of (020) at 4.51 \AA , (003) at 3.32 \AA and (060) at 1.52 \AA (Fig. 5). The peaks remain unchanged after glycolation and heating at 400 $^{\circ}\text{C}$. The peaks appear sharp, narrow and intense in all three modes of sample scanning, even though they exhibit broad bases. The 3.66 \AA peak at $11\bar{2}$ and the 3.09 \AA peak at 112 reflections are absent. A minor coexisting peak of illite is observed at 5.05 \AA (001 reflection) and 1.50 \AA at (060 reflection) (Fig. 5).

The prominent peak at 10.04 \AA (001) basal reflection along with the (020) reflection at 4.51 \AA (003) reflection at 3.33 \AA and (060) reflection at 1.52 \AA are characteristic of glauconite (Odin & Matter, 1981; Odom, 1984). Unmoved (001) reflection after glycolation and heating and the absence of $11\bar{2}$ and 112 reflections suggest negligible inter-stratification between expandable and non-expandable layers (Thompson & Hower, 1975). Glauconite in the Bryozoan Limestone Formation may be described as 'highly-evolved to evolved' type, containing ~10 % expandable layers, corresponding to ~8 % K_2O content (Odom, 1984) which are clearly different from clay minerals of verdine facies (cf. Harding *et al.* 2014).

4.d. Mössbauer spectroscopic study of glauconite

The Mössbauer spectrum of the glauconite sample indicates three symmetric doublets (Fig. 6). Doublets A and C, with isomer shift (δ) value $\delta = 0.33$ and 0.37 mm s^{-1} respectively, correspond to ferric ions, and doublet B ($\delta = 1.01 \text{ mm s}^{-1}$) indicates ferrous ions (Table 1). The doublet with the smaller quadrupole splitting (ΔEQ) is assigned to the less distorted cis-M (2) position whereas

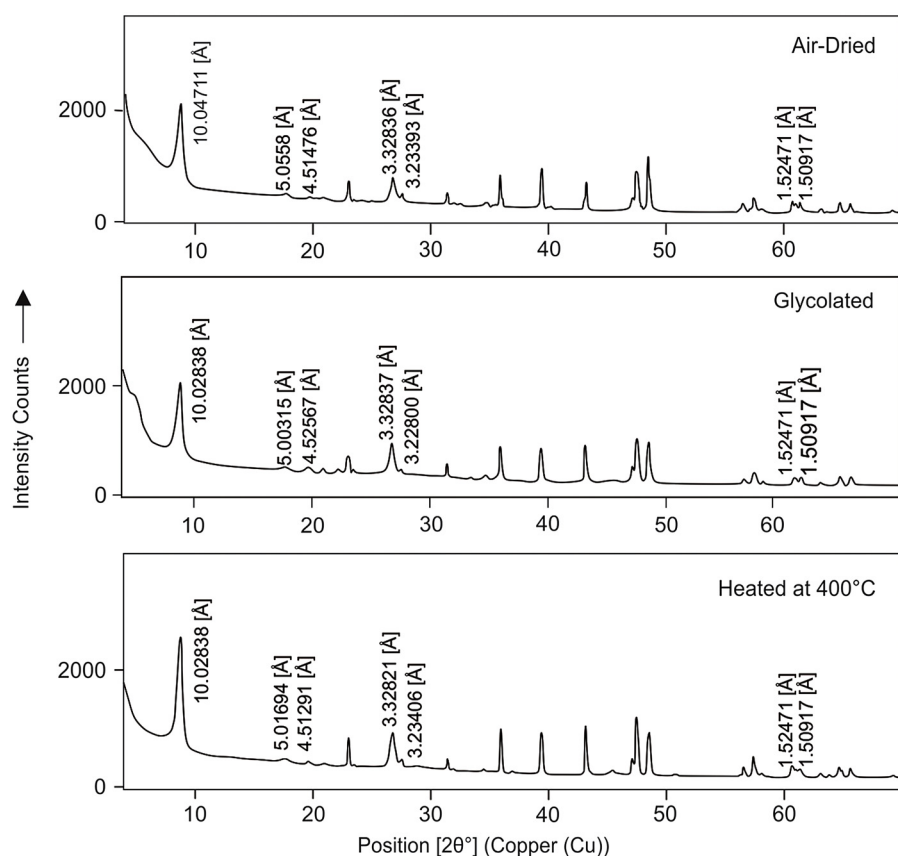


Fig. 5. XRD diffractograms of a glauconite sample under different conditions: air-dried, glycolated and heating at 400 °C.

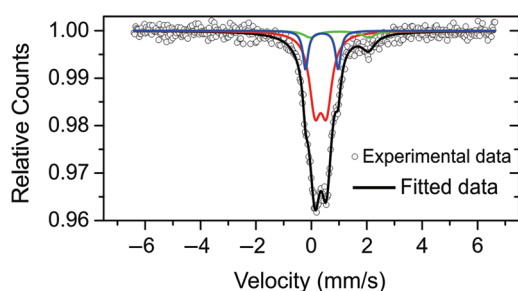


Fig. 6. (Colour online) Mössbauer spectrum of glauconite sample RT-8 recorded at room temperature indicating the relative abundance of Fe^{3+} (red and blue doublet) and Fe^{2+} (green doublet) cations.

the doublet with the larger quadrupole splitting is assigned to Fe^{3+} ions in the trans-M (1) position (Hogg & Meads, 1970; Rolf *et al.* 1977; McConchie *et al.* 1979; Kotlicki *et al.* 1981). The ΔEQ has a lower value for doublet A ($\Delta\text{EQ} = 0.415 \text{ mm s}^{-1}$) than for doublet C (1.18 mm s^{-1}). Therefore, doublet A is assigned to ferric ions in the cis-M (2) position, and doublet B is assigned to ferric ions in the trans-M (1) position. Doublet D belongs to ferrous ions and it has a high ΔEQ value equal to 2.105 mm s^{-1} , corresponding to the trans-M (1) position (octahedral site). The $\text{Fe}^{2+}/\text{Fe}^{3+}$ ratio of glauconite was calculated by taking into consideration the χ^2 value (fitting parameter) and the relative area (under curve) of the component belonging to the cationic composition of the octahedral sheets. The average $\text{Fe}^{2+}/\text{Fe}^{3+}$ ratio obtained by the Mössbauer spectroscopic study of glauconite is 0.12 (Table 1).

4.e. Major element composition of glauconite

Electron Probe Micro Analysis (EPMA) data of both varieties of glauconites in the Bryozoa Limestone Formation are provided in Table 2. All analyses were normalized to 100 wt % on an anhydrous basis for different cross-plots. The K_2O content of glauconites varies from 6.13 % to 8.16 %, suggesting ‘evolved’ to ‘highly evolved’ stage of maturation (Odin & Matter, 1981; Amorosi, 1997). The Fe_2O_3 (total) content of glauconite varies from 13.89 % to 20.48 %. The Al_2O_3 content of the glauconite is a bit higher than usual, varying from 8.00 % to 12.03 % (Odin & Matter, 1981). The MgO content of glauconite is also slightly higher than the average, varying from 3.24 % to 4.48 % (cf. Odin & Matter, 1981; Banerjee *et al.* 2016b). The CaO content of all varieties of glauconites is negligible, mostly ~ 1 % (av. 0.49 %). The SiO_2 content of glauconite varies from 48.79 % to 54.98 %. The mineral geochemistry of glauconite in Bryozoa Limestone Formation is therefore characterized by high K, high Si, high Mg, high Al and moderate Fe contents (Odin & Matter, 1981; Banerjee *et al.* 2016b). Similar compositions of glauconite are reported from the shallow-marine originated Kurnub Group (Jarrar *et al.* 2000) and the Nice Arc region (Pasquini *et al.* 2004). In contrast, Baldermann *et al.* (2017) reported the deep marine glauconite of the Ivory Coast – Ghana Marginal Ridge as containing high Fe, low Al and K.

The average $\text{Fe}^{2+}/\text{Fe}^{3+}$ ratio (0.12) obtained by the Mössbauer spectroscopic study was used for calculation of octahedral and tetrahedral charge as well as the structural formula of all the glauconite (Table 3). All data plot within the field of glauconite in the cross-plot of $4\text{M}^+/\text{Si}$ (M^+ = interlayered cations) vs $(\text{Fe octahedral})/(\text{Sum of octahedral charge})$ (cf. Meunier & El Albani,

Table 1. Computer-fitted Mössbauer spectral parameters of selected glauconite sample (RT-8)

Sample	Iron sites	Isomer shift (δ) (mm s ⁻¹) ± 0.06	Quadrupole splitting (Δ) (mm s ⁻¹) ± 0.11	Line width (Γ) (mm s ⁻¹) ± 0.11	Relative area (R_A) (%)	Ratio Fe ²⁺ /Fe ³⁺	Fitting quality (χ^2)
RT-8	A (Fe ³⁺) (Oct.)	0.34	0.42	0.49	79.8		
	B (Fe ²⁺) (Oct.)	1.01	2.11	0.59	10.8	0.12	0.98
	C (Fe ³⁺) (Oct.)	0.38	1.18	0.23	9.4		

Table 2. Oxide weight percentage of glauconite in the Bryozoa Limestone Formation

Bagh	SiO ₂	Al ₂ O ₃	Fe ₂ O ₃ (T)	MgO	MnO	CaO	K ₂ O	Na ₂ O	P ₂ O ₅	Total	
Glauconitized feldspars											
RT-7	54.21	12.03	15.77	3.74	0.00	0.27	6.22	0.63	0.07	93.18	
	50.12	10.39	15.70	3.77	0.02	0.30	6.69	0.18	0.00	87.30	
	54.10	11.88	15.39	3.50	0.00	0.31	6.13	0.35	0.04	91.80	
	49.94	9.14	15.91	3.24	0.07	0.50	6.28	0.08	0.09	85.26	
	52.02	9.34	15.97	3.42	0.03	0.50	6.29	0.09	0.03	87.70	
	50.63	9.74	16.55	3.74	0.04	0.73	6.36	0.08	0.01	87.87	
	50.63	9.28	16.69	3.51	0.05	0.48	6.61	0.03	0.00	87.27	
	51.27	8.55	19.35	3.89	0.03	0.45	7.79	0.05	0.01	91.39	
	51.58	9.49	16.13	3.60	0.07	0.77	6.84	0.14	0.00	88.62	
	50.27	8.65	19.36	4.11	0.09	0.50	7.82	0.04	0.02	90.87	
	52.73	11.13	13.89	4.23	0.12	1.00	6.27	0.08	0.04	89.46	
	49.70	8.66	16.26	3.67	0.00	0.42	6.75	0.03	0.03	85.51	
	RT-8	52.28	8.47	17.22	4.19	0.08	0.28	7.52	0.02	0.00	90.17
		49.74	8.28	20.48	3.75	0.04	0.49	7.94	0.14	0.04	91.36
	54.98	9.63	17.15	3.92	0.02	0.45	7.85	0.01	0.03	94.13	
	50.03	8.25	17.95	3.64	0.09	0.47	7.04	0.07	0.04	87.57	
	48.79	8.16	17.09	3.72	0.08	0.63	7.12	0.06	0.03	85.68	
	49.62	8.13	17.52	3.74	0.05	0.72	6.93	0.06	0.21	86.98	
	49.75	8.42	17.89	3.74	0.07	0.58	7.47	0.09	0.03	88.04	
	49.46	8.00	18.36	3.60	0.04	0.66	7.27	0.05	0.01	87.45	
RT-9	50.11	10.79	14.36	3.50	0.05	0.55	7.02	0.35	0.00	86.97	
	51.98	8.23	18.49	4.20	0.09	0.27	7.73	0.26	0.02	91.49	
Glauconite infillings											
RT-7	54.32	9.54	17.41	4.04	0.10	0.32	6.90	0.05	0.01	92.68	
	50.75	9.31	17.67	3.45	0.01	0.61	7.05	0.06	0.00	88.90	
	49.52	9.73	15.55	3.68	0.04	0.40	6.24	0.12	0.01	85.27	
	54.43	9.07	19.48	3.86	0.01	0.41	7.63	0.02	0.01	94.91	
	50.27	11.05	14.54	3.24	0.01	0.48	6.13	0.23	0.00	86.14	
	50.61	8.55	16.25	3.93	0.05	0.61	6.64	0.07	0.00	86.71	
	50.91	8.48	16.52	3.92	0.09	0.63	7.08	0.06	0.00	87.69	
	53.08	9.06	18.06	4.09	0.04	0.64	7.18	0.05	0.00	92.21	
RT-8	49.83	9.22	15.89	3.54	0.07	0.40	7.31	0.19	0.03	86.62	
RT-9	53.26	8.27	19.33	4.04	0.07	0.25	8.16	0.21	0.00	93.73	
	53.16	7.95	19.89	3.80	0.05	0.25	8.04	0.22	0.00	93.42	
	51.66	7.65	19.70	4.48	0.17	0.63	8.16	0.27	0.04	92.89	

Table 3. Structural composition of glauconite in the Bryozoan Limestone Formation

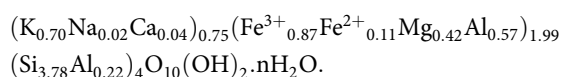
Substrate/ sample no.	Structural formulae	Tetrahedral charge	Octahedral R ³⁺
Glauconitized feldspars			
RT-6	(K _{0.78} Na _{0.01} Ca _{0.05}) _{0.84} (Fe ³⁺ _{1.10} Fe ²⁺ _{0.15} Mg _{0.48} Mn _{0.00} Al _{0.25}) _{1.98}	0.20	1.35
	(Si _{3.80} Al _{0.20}) ₄ O ₁₀ (OH) ₂ . n H ₂ O		
	(K _{0.81} Na _{0.00} Ca _{0.04}) _{0.85} (Fe ³⁺ _{1.09} Fe ²⁺ _{0.15} Mg _{0.50} Mn _{0.01} Al _{0.24}) _{1.99}	0.20	1.33
	(Si _{3.80} Al _{0.20}) ₄ O ₁₀ (OH) ₂ . n H ₂ O		
	(K _{0.58} Na _{0.01} Ca _{0.08}) _{0.67} (Fe ³⁺ _{0.68} Fe ²⁺ _{0.09} Mg _{0.46} Mn _{0.01} Al _{0.77}) _{2.00}	0.18	1.45
	(Si _{3.82} Al _{0.18}) ₄ O ₁₀ (OH) ₂ . n H ₂ O		
RT-7	(K _{0.66} Na _{0.00} Ca _{0.03}) _{0.70} (Fe ³⁺ _{0.84} Fe ²⁺ _{0.11} Mg _{0.42} Mn _{0.00} Al _{0.61}) _{1.99}	0.17	1.45
	(Si _{3.83} Al _{0.17}) ₄ O ₁₀ (OH) ₂ . n H ₂ O		
	(K _{0.66} Na _{0.00} Ca _{0.03}) _{0.70} (Fe ³⁺ _{0.84} Fe ²⁺ _{0.11} Mg _{0.42} Mn _{0.00} Al _{0.61}) _{1.99}	0.17	1.45
	(Si _{3.83} Al _{0.17}) ₄ O ₁₀ (OH) ₂ . n H ₂ O		
	(K _{0.55} Na _{0.09} Ca _{0.02}) _{0.66} (Fe ³⁺ _{0.74} Fe ²⁺ _{0.10} Mg _{0.39} Mn _{0.00} Al _{0.78}) _{2.01}	0.21	1.52
	(Si _{3.79} Al _{0.21}) ₄ O ₁₀ (OH) ₂ . n H ₂ O		
	(K _{0.64} Na _{0.03} Ca _{0.02}) _{0.69} (Fe ³⁺ _{0.79} Fe ²⁺ _{0.11} Mg _{0.42} Mn _{0.00} Al _{0.69}) _{2.01}	0.23	1.48
	(Si _{3.77} Al _{0.23}) ₄ O ₁₀ (OH) ₂ . n H ₂ O		
	(K _{0.55} Na _{0.05} Ca _{0.02}) _{0.62} (Fe ³⁺ _{0.73} Fe ²⁺ _{0.10} Mg _{0.37} Mn _{0.00} Al _{0.81}) _{2.00}	0.18	1.52
	(Si _{3.82} Al _{0.18}) ₄ O ₁₀ (OH) ₂ . n H ₂ O		
	(K _{0.68} Na _{0.07} Ca _{0.03}) _{0.77} (Fe ³⁺ _{0.81} Fe ²⁺ _{0.11} Mg _{0.44} Mn _{0.00} Al _{0.62}) _{1.98}	0.18	1.43
	(Si _{3.82} Al _{0.18}) ₄ O ₁₀ (OH) ₂ . n H ₂ O		
	(K _{0.61} Na _{0.01} Ca _{0.06}) _{0.68} (Fe ³⁺ _{0.83} Fe ²⁺ _{0.11} Mg _{0.42} Mn _{0.00} Al _{0.64}) _{2.00}	0.22	1.47
	(Si _{3.78} Al _{0.22}) ₄ O ₁₀ (OH) ₂ . n H ₂ O		
	(K _{0.64} Na _{0.00} Ca _{0.04}) _{0.68} (Fe ³⁺ _{0.84} Fe ²⁺ _{0.11} Mg _{0.39} Mn _{0.00} Al _{0.64}) _{1.99}	0.19	1.48
	(Si _{3.81} Al _{0.19}) ₄ O ₁₀ (OH) ₂ . n H ₂ O		
	(K _{0.73} Na _{0.01} Ca _{0.04}) _{0.77} (Fe ³⁺ _{0.95} Fe ²⁺ _{0.13} Mg _{0.42} Mn _{0.00} Al _{0.49}) _{2.00}	0.25	1.44
	(Si _{3.75} Al _{0.25}) ₄ O ₁₀ (OH) ₂ . n H ₂ O		
	(K _{0.65} Na _{0.02} Ca _{0.06}) _{0.73} (Fe ³⁺ _{0.80} Fe ²⁺ _{0.11} Mg _{0.40} Mn _{0.00} Al _{0.65}) _{1.97}	0.18	1.45
	(Si _{3.82} Al _{0.18}) ₄ O ₁₀ (OH) ₂ . n H ₂ O		
	(K _{0.74} Na _{0.01} Ca _{0.04}) _{0.78} (Fe ³⁺ _{0.96} Fe ²⁺ _{0.13} Mg _{0.45} Mn _{0.01} Al _{0.47}) _{2.02}	0.28	1.43
	(Si _{3.72} Al _{0.28}) ₄ O ₁₀ (OH) ₂ . n H ₂ O		
	(K _{0.82} Na _{0.00} Ca _{0.05}) _{0.87} (Fe ³⁺ _{1.08} Fe ²⁺ _{0.14} Mg _{0.52} Mn _{0.00} Al _{0.24}) _{1.99}	0.20	1.32
	(Si _{3.80} Al _{0.20}) ₄ O ₁₀ (OH) ₂ . n H ₂ O		
RT-8	(K _{0.70} Na _{0.00} Ca _{0.02}) _{0.73} (Fe ³⁺ _{0.85} Fe ²⁺ _{0.11} Mg _{0.46} Mn _{0.00} Al _{0.57}) _{2.00}	0.16	1.42
	(Si _{3.84} Al _{0.16}) ₄ O ₁₀ (OH) ₂ . n H ₂ O		
	(K _{0.75} Na _{0.02} Ca _{0.04}) _{0.81} (Fe ³⁺ _{1.02} Fe ²⁺ _{0.14} Mg _{0.42} Mn _{0.00} Al _{0.42}) _{2.00}	0.30	1.44
	(Si _{3.70} Al _{0.30}) ₄ O ₁₀ (OH) ₂ . n H ₂ O		
	(K _{0.71} Na _{0.01} Ca _{0.05}) _{0.77} (Fe ³⁺ _{0.89} Fe ²⁺ _{0.12} Mg _{0.43} Mn _{0.01} Al _{0.54}) _{1.98}	0.21	1.43
	(Si _{3.79} Al _{0.21}) ₄ O ₁₀ (OH) ₂ . n H ₂ O		
	(K _{0.68} Na _{0.01} Ca _{0.06}) _{0.74} (Fe ³⁺ _{0.90} Fe ²⁺ _{0.12} Mg _{0.43} Mn _{0.00} Al _{0.53}) _{1.98}	0.20	1.43
	(Si _{3.80} Al _{0.20}) ₄ O ₁₀ (OH) ₂ . n H ₂ O		
	(K _{0.72} Na _{0.01} Ca _{0.05}) _{0.78} (Fe ³⁺ _{0.91} Fe ²⁺ _{0.12} Mg _{0.42} Mn _{0.00} Al _{0.52}) _{1.98}	0.23	1.43
	(Si _{3.77} Al _{0.23}) ₄ O ₁₀ (OH) ₂ . n H ₂ O		
	(K _{0.71} Na _{0.01} Ca _{0.05}) _{0.77} (Fe ³⁺ _{0.94} Fe ²⁺ _{0.13} Mg _{0.41} Mn _{0.00} Al _{0.52}) _{1.98}	0.23	1.46
	(Si _{3.78} Al _{0.23}) ₄ O ₁₀ (OH) ₂ . n H ₂ O		

(Continued)

Table 3. (Continued)

Substrate/ sample no.	Structural formulae	Tetrahedral charge	Octahedral R ³⁺
RT-9	(K _{0.68} Na _{0.05} Ca _{0.04}) _{0.77} (Fe ³⁺ _{0.73} Fe ²⁺ _{0.10} Mg _{0.39} Mn _{0.00} Al _{0.74}) _{1.97}	0.22	1.47
	(Si _{3.78} Al _{0.22}) ₄ O ₁₀ (OH) ₂ · n H ₂ O		
	(K _{0.72} Na _{0.04} Ca _{0.02}) _{0.78} (Fe ³⁺ _{0.91} Fe ²⁺ _{0.12} Mg _{0.46} Mn _{0.01} Al _{0.50}) _{2.00}	0.20	1.41
	(Si _{3.80} Al _{0.20}) ₄ O ₁₀ (OH) ₂ · n H ₂ O		
Glauconite infillings			
RT-7	(K _{0.67} Na _{0.01} Ca _{0.05}) _{0.73} (Fe ³⁺ _{0.88} Fe ²⁺ _{0.12} Mg _{0.38} Mn _{0.00} Al _{0.60}) _{1.98}	0.22	1.48
	(Si _{3.78} Al _{0.22}) ₄ O ₁₀ (OH) ₂ · n H ₂ O		
	(K _{0.61} Na _{0.02} Ca _{0.03}) _{0.66} (Fe ³⁺ _{0.80} Fe ²⁺ _{0.11} Mg _{0.42} Mn _{0.00} Al _{0.68}) _{2.01}	0.20	1.48
	(Si _{3.80} Al _{0.20}) ₄ O ₁₀ (OH) ₂ · n H ₂ O		
	(K _{0.68} Na _{0.00} Ca _{0.03}) _{0.71} (Fe ³⁺ _{0.91} Fe ²⁺ _{0.12} Mg _{0.40} Mn _{0.00} Al _{0.55}) _{1.99}	0.20	1.46
	(Si _{3.80} Al _{0.20}) ₄ O ₁₀ (OH) ₂ · n H ₂ O		
	(K _{0.59} Na _{0.03} Ca _{0.04}) _{0.66} (Fe ³⁺ _{0.74} Fe ²⁺ _{0.10} Mg _{0.37} Mn _{0.00} Al _{0.78}) _{1.99}	0.20	1.52
	(Si _{3.80} Al _{0.20}) ₄ O ₁₀ (OH) ₂ · n H ₂ O		
	(K _{0.64} Na _{0.01} Ca _{0.05}) _{0.70} (Fe ³⁺ _{0.83} Fe ²⁺ _{0.11} Mg _{0.44} Mn _{0.00} Al _{0.60}) _{1.99}	0.16	1.43
	(Si _{3.84} Al _{0.16}) ₄ O ₁₀ (OH) ₂ · n H ₂ O		
	(K _{0.68} Na _{0.01} Ca _{0.05}) _{0.74} (Fe ³⁺ _{0.84} Fe ²⁺ _{0.11} Mg _{0.44} Mn _{0.01} Al _{0.59}) _{1.98}	0.17	1.43
	(Si _{3.83} Al _{0.17}) ₄ O ₁₀ (OH) ₂ · n H ₂ O		
	(K _{0.66} Na _{0.01} Ca _{0.05}) _{0.71} (Fe ³⁺ _{0.87} Fe ²⁺ _{0.12} Mg _{0.44} Mn _{0.00} Al _{0.57}) _{2.00}	0.20	1.44
	(Si _{3.80} Al _{0.20}) ₄ O ₁₀ (OH) ₂ · n H ₂ O		
RT-8	(K _{0.71} Na _{0.03} Ca _{0.03}) _{0.77} (Fe ³⁺ _{0.82} Fe ²⁺ _{0.11} Mg _{0.40} Mn _{0.00} Al _{0.64}) _{1.97}	0.19	1.46
	(Si _{3.81} Al _{0.19}) ₄ O ₁₀ (OH) ₂ · n H ₂ O		
	(K _{0.74} Na _{0.03} Ca _{0.02}) _{0.79} (Fe ³⁺ _{0.93} Fe ²⁺ _{0.12} Mg _{0.43} Mn _{0.00} Al _{0.5}) _{1.98}	0.20	1.43
	(Si _{3.80} Al _{0.20}) ₄ O ₁₀ (OH) ₂ · n H ₂ O		
RT-9	(K _{0.74} Na _{0.03} Ca _{0.02}) _{0.79} (Fe ³⁺ _{0.96} Fe ²⁺ _{0.13} Mg _{0.41} Mn _{0.00} Al _{0.48}) _{1.97}	0.19	1.44
	(Si _{3.81} Al _{0.19}) ₄ O ₁₀ (OH) ₂ · n H ₂ O		
	(K _{0.76} Na _{0.04} Ca _{0.05}) _{0.84} (Fe ³⁺ _{0.96} Fe ²⁺ _{0.13} Mg _{0.48} Mn _{0.01} Al _{0.41}) _{1.99}	0.25	1.37
	(Si _{3.75} Al _{0.25}) ₄ O ₁₀ (OH) ₂ · n H ₂ O		
	(K _{0.62} Na _{0.01} Ca _{0.02}) _{0.65} (Fe ³⁺ _{0.83} Fe ²⁺ _{0.11} Mg _{0.43} Mn _{0.01} Al _{0.64}) _{2.01}	0.16	1.47
	(Si _{3.84} Al _{0.16}) ₄ O ₁₀ (OH) ₂ · n H ₂ O		

2007) (Fig. 7). The average formula of the glauconite in the Bryozoan Limestone is



4.f. Concentrations of REE in Glauconite

Total REE concentrations of glauconite remain similar in all the samples (Table 4). The concentration of Σ LREE is higher (avg. 46.57 ppm) than Σ HREE (avg. 4.23 ppm). Chondrite-normalized pattern reveals moderate light-REE (LREE)/heavy-REE (HREE) fractionation (9.70 to 13.01) and very weak negative Eu anomaly (Fig. 8a). The PAAS (Post-Archean Australian Shale)-normalized pattern exhibit a 'hat-shape' with a negative Ce anomaly and a moderately positive Eu anomaly (Fig. 8b). The hat-shape of the PAAS-normalized - REE pattern is characteristic of authigenic glauconite

(cf. Jarrar *et al.* 2000; Banerjee *et al.* 2012a, b; Bansal *et al.* 2018). Glauconite samples occupy both IIb and IIIb fields in the Ce anomaly vs Pr anomaly (Pr/Pr*) cross-plot of Bau & Dulski (1996) (Fig. 8c). The samples plotting in the IIIb field correctly indicate the palaeo-redox condition (cf. Bau & Dulski, 1996). The true negative Ce anomaly reflects a sub-oxic condition of the early diagenetic environment (cf. Elderfield & Pagett, 1986; Wright *et al.* 1987; Fig. 7d). Nd concentrations of glauconite (9.05–9.17 ppm) suggest moderate sedimentation rate (cf. Wright *et al.* 1987; Fig. 8d; Table 4).

5. Discussion

The early diagenetic glauconite in the Bryozoan Limestone Formation occurs as stringers within feldspars. Textural evidences indicate that glauconite replaces K-feldspars (Banerjee *et al.* 2008, 2015; Bansal *et al.* 2017, 2018). The evolutionary trend of glauconite within the Bryozoan Limestone Formation neither supports the 'verdissement' nor 'layer lattice' theory as the K₂O contents of

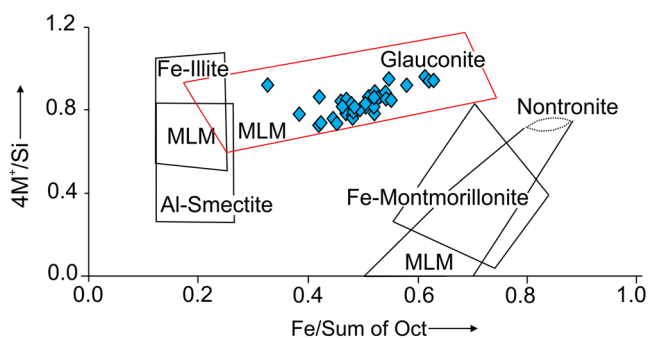


Fig. 7. (Colour online) Cross-plot of $(4M^*)/Si$ (M = interlayered cations) vs $(Fe \text{ octahedral})/(\text{Sum of octahedral charge})$ (original plot after Meunier & El Albani, 2007).

glauconites are consistently high. The high K_2O content of glauconite, moderate Fe_2O_3 (total) and textural evidences corroborate the replacement of K-feldspar (Banerjee *et al.* 2015; Bansal *et al.* 2017, 2018). The Fe_2O_3 (total) content of glauconite in the Bryozoa Limestone Formation varies from 13.89 % to 20.48 %, averaging 17.19 %. The rate of sedimentation, palaeo-redox condition, composition of substrate, microenvironment within the substrate and surrounding sediment determines the Fe_2O_3 (total) content (Odin & Matter, 1981; Meunier & El Albani, 2007; Banerjee *et al.* 2016b; Baldermann *et al.* 2017; Tang *et al.* 2017). The sub-oxic condition of the Bryozoa Limestone Formation resulted in mobility of Fe ions. The moderate Fe_2O_3 (total) content emplaced into the glauconite structure possibly related to a moderate rate of sedimentation (Baldermann *et al.* 2017). The Al_2O_3 content of the glauconite remained high because of its availability in the shallow marine environment and Al-Fe substitution in the glauconite structure. The Bryozoa Limestone glauconite formed in shallow sea surrounded by cratonic areas. Detrital siliciclastics delivered from these cratonic areas provided additional cations like Si, Al, Fe and K. A combination of moderate Fe_2O_3 and high Al_2O_3 , SiO_2 and K_2O , therefore, characterizes shallow marine glauconite formed in sub-oxic conditions under moderate sedimentation rate. Deep marine glauconite, forming at a lower temperature, usually exhibits a high Fe_2O_3 , low Al_2O_3 and a five times slower sedimentation rate compared to shallow marine glauconite.

In a recent review, Banerjee *et al.* (2016b) reported an unusually high abundance of glauconite corresponding to greenhouse climates in the Early Cretaceous, Late Cretaceous and Eocene epochs. This study focuses upon the abundance of glauconite in the Late Cretaceous Epoch and explores possible reasons for it (Fig. 9). Haq (2014) reported consistently high sea level during the Late Cretaceous Epoch, with the highest peak during the Turonian, ~240–250 m above the present-day mean sea level. The Haq curve also displays two ~20 Ma long periods of relatively high and stable sea levels (Aptian through Early Albian and Coniacian through Campanian). Our review suggests that the highest degree of glauconite enrichment occurred during the Cenomanian, followed by Turonian, Coniacian, Campanian and Maastrichtian (Fig. 9; Table 5). The Late Cretaceous glauconites are traced all along the margins of Tethys (Fig. 10). Local conditions such as freshwater input may influence the formation of authigenic glauconite within basins (El Albani *et al.* 2005; Bansal *et al.* 2018). However, the widespread occurrence of glauconite across the Tethyan margin suggests broadly similar palaeo-depositional conditions. Most of these Late Cretaceous, Tethyan margin glauconites formed in a shallow marine environment (Garrison *et al.* 1987; Glenn & Arthur, 1990; Carson & Crowley, 1993; Amireh *et al.* 1998;

Table 4. REE concentrations of selected glauconites in the Bryozoa Limestone Formation

Sample name	units	blank	RT-4	RT-7	RT-8
weight	mg	NA	25.2	25.2	25.5
solvent vol.	mL	25.00	25.00	25.00	25.00
La	ppm	0.00	11.20	10.26	11.65
Ce	ppm	0.00	20.22	17.27	22.03
Pr	ppm	0.00	2.59	2.33	2.45
Nd	ppm	0.00	9.17	9.05	9.07
Sm	ppm	0.00	1.75	1.83	1.90
Eu	ppm	0.00	0.44	0.52	0.48
Gd	ppm	0.00	1.86	1.97	1.89
Tb	ppm	0.00	0.26	0.29	0.30
Dy	ppm	0.00	1.50	1.66	1.74
Ho	ppm	0.00	0.29	0.35	0.35
Er	ppm	0.00	0.80	1.00	1.04
Tm	ppm	0.00	0.10	0.14	0.15
Yb	ppm	0.00	0.59	0.88	0.90
Lu	ppm	0.00	0.09	0.14	0.13
Y	ppm	0.00	8.68	10.19	9.46
Total REE	N.A.	N.A.	50.86	47.67	53.86
Σ LREE	N.A.	N.A.	47.23	43.21	54.08
Σ HREE	N.A.	N.A.	3.63	4.45	49.47
LREE/HREE	N.A.	N.A.	13.01	9.70	10.73
Eu/Eu*	N.A.	N.A.	0.26	0.29	0.26
Pr/Pr*	N.A.	N.A.	1.08	1.05	0.99
Ce/Ce*	N.A.	N.A.	0.86	0.81	0.94
Log (Ce/Ce*)	N.A.	N.A.	-0.06	-0.09	-0.02

Pasquini *et al.* 2004; Martinec *et al.* 2010; Tewari *et al.* 2010; Yilmaz *et al.* 2012; Zalat *et al.* 2012). However, the sharp decline in the abundance of glauconite across the Cretaceous/Tertiary boundary and the shift of its depositional setting to deep marine (Amouric & Parron, 1985; Parron & Amouric, 1990) indicates an unusual seawater composition of the Late Cretaceous Tethys. The seawater during the Late Cretaceous Epoch was warm; palaeoclimate was humid with considerably high hydrothermal flux associated with elevated production of mid-oceanic ridges (Hardie, 1966; Demicco *et al.* 2005; Timofeeff *et al.* 2006). Lush growth of land vegetation led to increasing nutrient supply, enhanced organic productivity and oxygen depletion on the marine shelf. Enhanced biological productivity induced a sub-oxic depositional condition facilitating the formation of glauconite on shallow shelves (Ozaki & Tajika, 2013). Several studies recorded lateral transition of glauconitic sediments to organic-rich shales in deeper parts of the basin where conditions were anoxic (Parrish *et al.* 2001; Bansal *et al.* 2019). The 'greenhouse' condition of the Late Cretaceous Epoch increased the rate of shelf sedimentation and continental weathering. It can be assumed that, in consequence, concentrations of H_3SiO_4 , SO_4 , Cl, Na, Mg, K, Fe and other ions in seawater were elevated. Experimental investigations

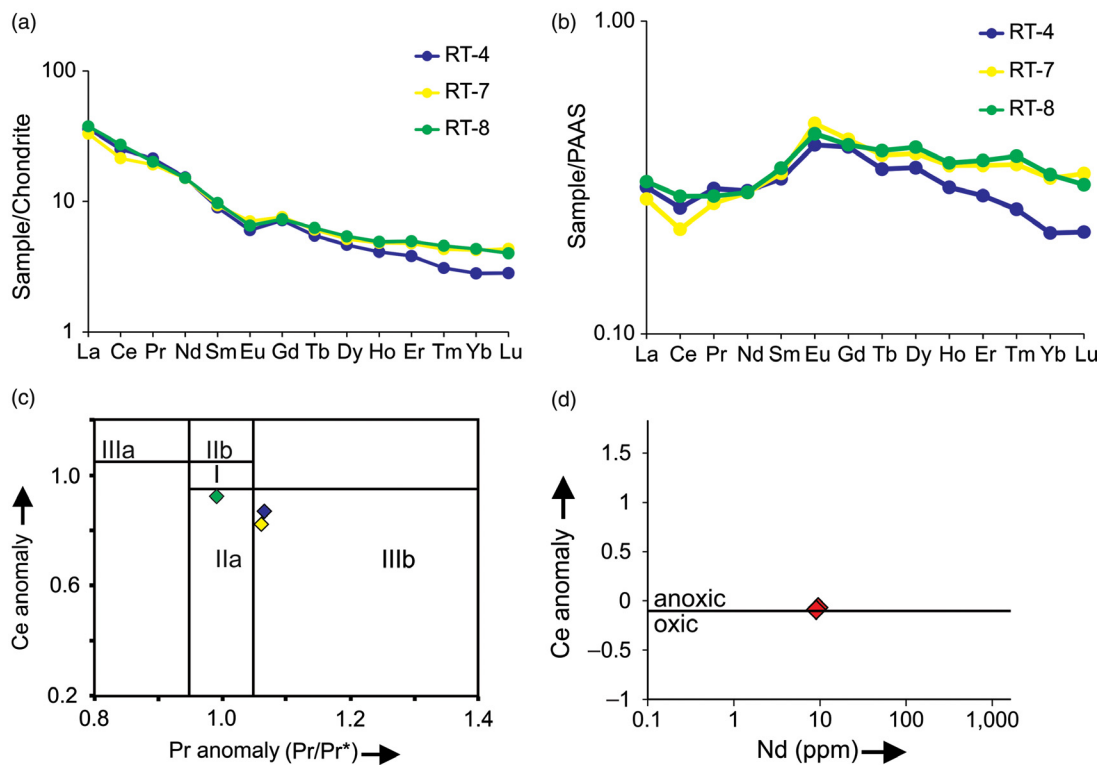


Fig. 8. (Colour online) (a) Chondrite-normalized and (b) PAAS-normalized REE patterns of glauconite; (c) cross-plot of (Ce/Ce^*) vs (Pr/Pr^*) in glauconites (after Bau & Dulski, 1996) (note two glauconite samples plotting in the IIIb field); (d) cross-plot of Ce anomaly and Nd concentrations (anoxic-oxic boundary is placed at -0.10 after Wright *et al.* 1987).

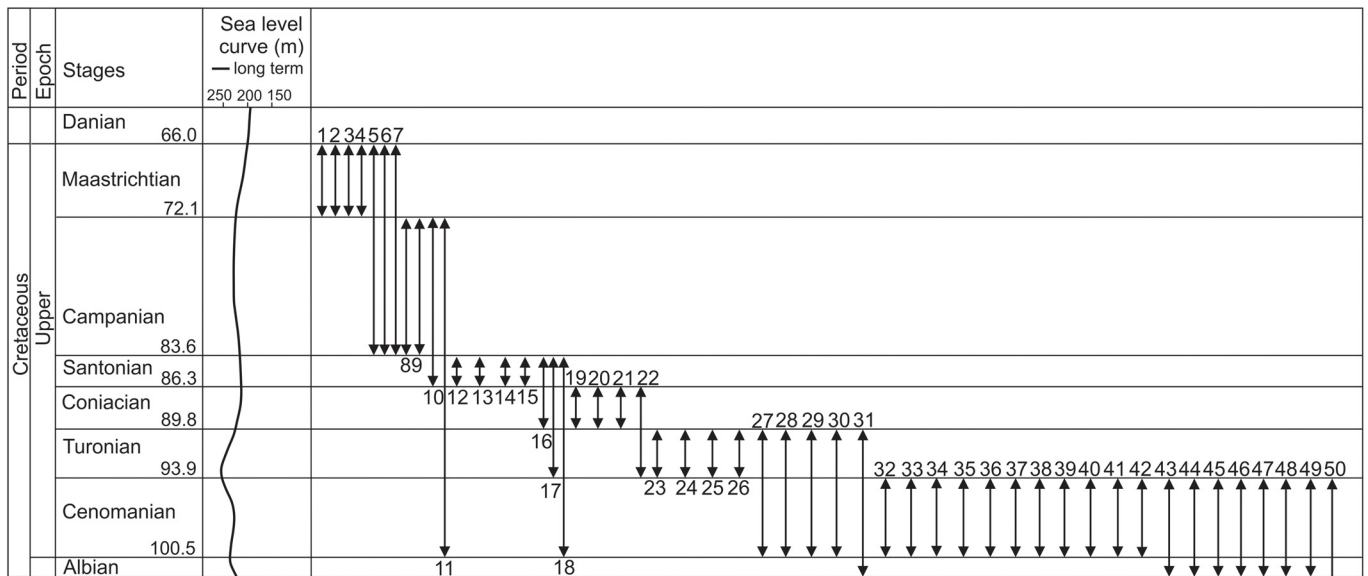


Fig. 9. (Colour online) Abundance of glauconite within the Upper Cretaceous. Note maximum abundance of glauconite in Cenomanian, followed by Turonian; Coniacian, Campanian and Maastrichtian exhibit similar, moderately abundant glauconite.

suggest abundant supply of K, Fe, Si and Mg favours glauconite formation on the seafloor (Harder, 1980). Chafetz & Reid (2000) rejected the requirement of slow rate of sedimentation for glauconite precipitation on the basis of sedimentary structures and textures in the Late Cambrian Morgan Creek Limestone.

Abundant occurrence of glauconite in the Late Cretaceous shallow shelves, therefore, can be related to the different seawater

composition, charged with high concentrations of Na, Mg, K, Fe, Si, Al and Ca and depleted in oxygen. Recently Tang *et al.* (2017) suggested a shallow redoxcline for shallow marine Precambrian glauconite. The glauconite within the Late Cretaceous Bryozoa Limestone Formation, therefore, supports the existence of a ‘glauconitic sea’ and attributes its widespread occurrence to unusual seawater composition across the Tethyan

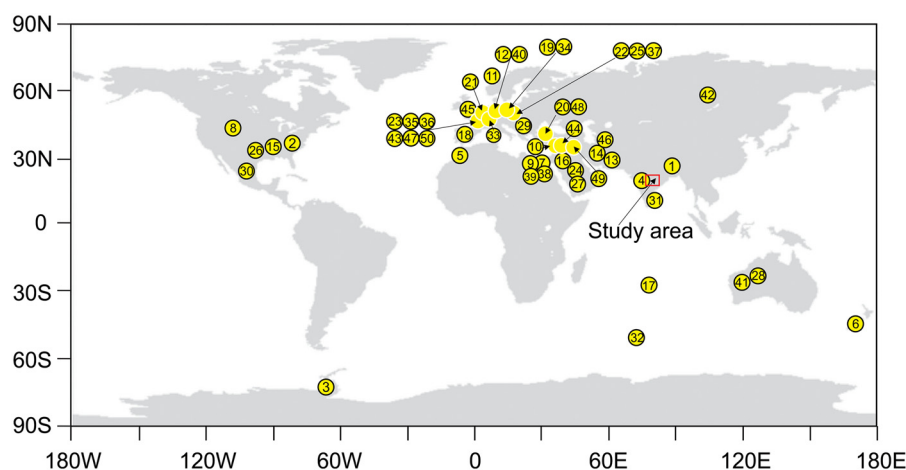
Table 5. Glauconite occurrences during Late Cretaceous with environmental interpretations

Age	Formation	Depositional environment	References
Maastrichtian	1) Mahadek Formation, India	shallow marine	Mishra & Sen (2001); Tewari <i>et al.</i> (2010)
Maastrichtian	2) Peedee Formation, Carolina	open marine shelf deposition	Harris & Bottino (1974); Harris (1976); Legrand (1989)
Maastrichtian	3) López de Bertodano Formation, Antarctic Peninsula	middle to outer shelf	Witts <i>et al.</i> (2015)
Maastrichtian	4) Lameta Formation, India	estuarine	Bansal <i>et al.</i> (2018)
Maastrichtian–Campanian	5) Tamezzakht succession, Morocco	deep marine	El Kadiri <i>et al.</i> (2005)
Maastrichtian–Campanian	6) Tahora Formation, New Zealand	outer shelf	Isaac <i>et al.</i> (1991)
Maastrichtian–Campanian	7) Duwi Formation, Egypt	shallow marine	Glenn & Arthur (1990); Baioumy (2007); Rifai & Shaaban (2007)
Campanian	8) Shannon sandstone, Wyoming	shoreface, shallow marine	Walker & Bergman (1993); Amorosi (2011)
Campanian	9) Qusseir Formation, Egypt	inner shelf	Khalifa (1983); Baioumy & Boulis (2012a)
Campanian–Santonian	10) Menuha Formation, Israel	outer shelf	Retzler <i>et al.</i> (2013)
Campanian–Cenomanian	11) Svarte, Tryggvason, lower Kyrre Formation, Måløy Slope, offshore Norway	–	Prélat <i>et al.</i> (2015)
Santonian	12) Haltern Formation, Germany	shallow marine (40–60 m)	Banning <i>et al.</i> (2013)
Santonian	13) Neka Valley, Iran	deep marine (200–500 m)	Berra <i>et al.</i> (2007)
Santonian	14) Zagros, SW Iran	deep platform	Ghabeishavi <i>et al.</i> (2009)
Santonian	15) Tombigbee Sand Member, Eutaw Formation, Mississippi	open marine	Schwimmer <i>et al.</i> (1985)
Santonian–Coniacian	16) Matulla Formation, Egypt	lagoon/shoreface	El-Azabi & El-Araby (2007); Zalat <i>et al.</i> (2012); Farouk (2015)
Santonian–Turonian	17) Indian Ocean, Ocean Drilling Program leg 121 (Broken Ridge)	deep marine	Rea <i>et al.</i> (1990)
Santonian–Cenomanian	18) Sierra de Guadarrama Formation, central Spain	–	Amorosi <i>et al.</i> (2012)
Coniacian	19) Kraków Swell, Poland	shallow marine	Olszewska-Nejbert & Świerczewska-Gładysz (2013)
Coniacian	20) Karababa Formation, Turkey	shallow marine	Yılmaz <i>et al.</i> (2018)
Coniacian	21) NW Europe		Guinot (2013)
Coniacian–Turonian	22) Peruc–Korycany Formation, Czech Republic	shoreface	Caracciolo <i>et al.</i> (2011)
Turonian	23) Maine-et-Loire, France	–	Courbe <i>et al.</i> (1981)
Turonian	24) Kometan Formation, NE Iraq	open marine	Al-Sheikhly <i>et al.</i> (2015)
Turonian	25) Bíla Hora Formation, Bohemia, Czech Republic	open shelf	Čech <i>et al.</i> (2005); Žitt <i>et al.</i> (2015)
Turonian	26) Rubble Zone, Bouldin Creek outcrop, Texas		Stephenson (1929)
Turonian–Cenomanian	27) Raha Formation, Egypt	shallow marine	Anan (2014)
Turonian–Cenomanian	28) Darwin, Marligar, Wangarlu, Moonkinu formations, Australia	shallow marine	Henderson (1998)
Turonian–Cenomanian	29) Sv. Duh Formation, Ćićarija Mountain region (northern Istria, Croatia)	deep marine with open ocean interaction	Brčić <i>et al.</i> (2017)
Turonian–Cenomanian	30) Agua Nueva Formation, central Mexico	deep water	Núñez–Useche <i>et al.</i> (2016)
Turonian–Albian	31) Karai Shale Formation, India	deep marine (100–150 m)	Banerjee <i>et al.</i> (2016a)
Cenomanian	32) Ocean Drilling Program Site 1138, Kerguelen Plateau	nearshore, inner–outer shelf	Dickson <i>et al.</i> (2017)
Cenomanian	33) Kamm Bed (Garschella Formation), central Switzerland	deeper part of shelf	Westermann <i>et al.</i> (2010)

(Continued)

Table 5. (Continued)

Age	Formation	Depositional environment	References
Cenomanian	34) Wolbrom–Miechów area (southern Poland)	–	Salamon (2007)
Cenomanian	35) Section at Pays de Caux, Normandy, France	–	Selby (2009)
Cenomanian	36) Cormes and Villers Formation, France	–	Robert (1973)
Cenomanian	37) Zamel Sandstone, Bohemia, Czech Republic	shallow marine	Martinec <i>et al.</i> (2010)
Cenomanian	38) Baharaiya Formation, Egypt	inner shelf	Khalifa (1983); Baoumy & Boulis (2012b)
Cenomanian	39) Galala Formation, Galala Plateau, Egypt	shallow subtidal	Farouk (2015)
Cenomanian	40) Essen Greensands, Pläner Limestone, N Germany	near shore to middle shelf (20–100 m)	Wilmsen <i>et al.</i> (2005)
Cenomanian	41) Groote Eylandt Mn – deposit, Australia	outer shelf	Ostwald (1990)
Cenomanian	42) Melovatskaya Formation,	marine	Afanasjeva <i>et al.</i> (2013)
Cenomanian–Albian	43) SE Russia	–	Odin <i>et al.</i> (1977)
Cenomanian–Albian	44) Paris Basin, France	shallow marine	Amireh (1997); Amireh <i>et al.</i> (1998); Jarrar <i>et al.</i> (2000)
Cenomanian–Albian	45) Kurnub Group, Jordan	shallow marine	Garrison <i>et al.</i> (1987); Carson & Crowley (1993)
Cenomanian–Albian	46) Upper Greensand Formation and Beer Head Limestone, Devon, SW England	shoreface and outer shelf	Sharafi <i>et al.</i> (2013)
Cenomanian–Albian	47) Aitamir Formation, Kopet-Dagh Basin,	shelf	Rousset <i>et al.</i> (2004)
Cenomanian–Albian	48) Turkmenistan and Iran	shoreface to middle shelf	Varol <i>et al.</i> (2000)
Cenomanian–Albian	49) Dent de Marcoule, SE France	–	Al-Dabbas <i>et al.</i> (2012)
Cenomanian–Valanginian	50) Kilimli, Sapca and Cemaller formations, Turkey	shallow marine	Pasquini <i>et al.</i> (2004)


**Fig. 10.** (Colour online) Occurrence of Late Cretaceous glauconite. Note continuity of glauconite abundance across the Tethyan belt (reference number corresponds to that provided in Table 5).

belt. The shift of authigenic glauconite from shallow to deep water during the Post-Cretaceous time relates to increased oxygenation (Gale *et al.* 2001) in the shallow marine environment.

6. Conclusions

Glauconite formed in a shallow marine environment within the Late Cretaceous Bryozoa Limestone Formation. The Ce anomaly of glauconite confirms the existence of a sub-oxic diagenetic environment that limited the mobility of Fe ions into the glauconite

structure. The concentration of Nd indicates a moderate rate of background sedimentation. The seawater possessed a high Al_2O_3 , moderate Fe_2O_3 and moderately high Mg content. Extensive glauconite formation suggests prevalence of broadly similar chemical constraints all along the Late Cretaceous Tethyan belt. Enhanced organic productivity and elevated concentrations of Mg, K, Fe, Si and Al cations in low oxygenated seawater during the Late Cretaceous greenhouse climate favoured the formation of glauconite.

Author ORCIDs.  Santanu Banerjee, 0000-0002-9548-7047

Acknowledgements. The authors thank the Indian Institute of Technology Bombay (IITB) for infrastructure facilities. S.B. is thankful to Ministry of Mines, Government of India, for the financial support through grant F. No. 14/77/2015-Met IV. The authors thank SC Patel and Javed M Shaikh for analysis at the DST–IITB National Facility for EPMA, Department of Earth Sciences, IITB. Authors are thankful to anonymous reviewers for their suggestions on an earlier version of the manuscript.

References

- Afanasjeva NI, Zorina SO, Gubaidullina AM, Naumkina NI and Suchkova GG (2013) Crystal chemistry and genesis of glauconite from “Melovatka” section (Cenomanian, of South-Eastern Russian Plate). *Litosfera* **2**, 65–75.
- Ahmad AHM and Akhtar K (1990) Clastic environments and facies of the Lower Cretaceous Narmada Basin, India. *Cretaceous Research* **11**, 175–90.
- Akhtar K and Ahmad AHM (1991) Single-cycle cratonic quartzarenites produced by tropical weathering: The Nimar sandstone (Lower Cretaceous), Narmada basin, India. *Sedimentary Geology* **71**, 23–32.
- Akhtar K and Khan DA (1997) A tidal island model for carbonate sedimentation: Karondia Limestone of Cretaceous Narmada Basin. *Journal of the Geological Society of India* **50**, 481–90.
- Al-Dabbas MA, Jassim JA and Qaradaghi AI (2012) Sedimentological and depositional environment studies of the Maudud Formation, central and southern Iraq. *Arabian Journal of Geosciences* **5**, 297–312.
- Al-Sheikhly SS, Tamar-Agha MY and Mahdi MM (2015) The facies analysis of the Cenomanian–Turonian succession of Surdash–Shaqlawa area, NE. Iraq. *Iraqi Journal of Science* **56** I C, 767–73.
- Amireh BS (1997) Sedimentology and palaeogeography of the regressive transgressive Kurnub Group (Early Cretaceous) of Jordan. *Sedimentary Geology* **112**, 69–88.
- Amireh BS, Jarrar GH, Henjes-Kunst F and Schneider W (1998) K/Ar dating, X-ray diffractometry, optical and scanning electron microscopy of glauconites from the Early Cretaceous Kurnub Group of Jordan. *Geological Journal* **33**, 49–65.
- Amorosi A (1995) Glaucony and sequence stratigraphy: a conceptual framework of distribution in siliciclastic sequences. *Journal of Sedimentary Research* **65**, 419–25.
- Amorosi A (1997) Detecting compositional, spatial, and temporal attributes of glaucony: a tool for provenance research. *Sedimentary Geology* **109**, 135–53.
- Amorosi A, (2012) The occurrence of glauconite in the stratigraphic record: distribution patterns and stratigraphic significance. In *Linking Diagenesis to Sequence Stratigraphy* (eds S Morad, M Ketzer and LF De Ross), pp. 37–54. International Association of Sedimentologists, Special Publication no. 45.
- Amorosi A (2011) The problem of glaucony from the Shannon Sandstone (Campanian Wyoming). *Terra Nova* **23**, 100–7.
- Amorosi A and Centinco MC (1997) Glaucony from the Eocene of the Isle of Wight (southern UK): implications for basin analysis and sequence stratigraphic interpretation. *Journal of the Geological Society of London* **154**, 887–96.
- Amorosi A, Guidi R, Mas R and Falanga E (2012) Glaucony from the Cretaceous of the Sierra de Guadarrama (Central Spain) and its application in a sequence stratigraphic context. *International Journal of Earth Sciences* **1**, 415–27.
- Amouric M and Parron C (1985) Structure and growth mechanism of glauconite as seen by high resolution transmission electron microscopy. *Clays and Clay Minerals* **33**, 473–82.
- Anan TI (2014) Facies analysis and sequence stratigraphy of the Cenomanian–Turonian mixed siliciclastic–carbonate sediments in West Sinai, Egypt. *Sedimentary Geology* **307**, 34–46.
- Baioumy HM (2007) Iron–phosphorus relationship in the iron and phosphorite ores of Egypt. *Chemie der Erde* **67**, 229–39.
- Baioumy HM and Boulis SN (2012a) Glauconites from the Bahariya Oasis: an evidence for Cenomanian marine transgression in Egypt. *Journal of African Earth Sciences* **70**, 1–7.
- Baioumy HM and Boulis SN (2012b) Non-pelletal glauconites from the Campanian Quessir Formation, Egypt: implication for glauconitization. *Sedimentary Geology* **249**, 1–9.
- Baldermann A, Dietzel M, Mavromatis V, Mittermayr F, Warr LN and Wemmer K (2017) The role of Fe on the formation and diagenesis of interstratified glauconite–smectite and illite–smectite: a case study of Upper Cretaceous shallow-water carbonates. *Chemical Geology* **453**, 21–34.
- Banerjee S, Bansal U, Pande K and Meena SS (2016a) Compositional variability of glauconites within the Upper Cretaceous Karai Shale Formation, Cauvery Basin, India: implications for evaluation of stratigraphic condensation. *Sedimentary Geology* **331**, 12–29.
- Banerjee S, Bansal U and Thorat A (2016b) A review on palaeogeographic implications and temporal variation in glaucony composition. *Journal of Palaeogeography* **5**, 43–71.
- Banerjee S, Chattoraj SL, Saraswati PK, Dasgupta S and Sarkar U (2012a) Substrate control on formation and maturation of glauconites in the Middle Eocene Harudi Formation, western Kutch, India. *Marine and Petroleum Geology* **30**, 144–60.
- Banerjee S, Chattoraj SL, Saraswati PK, Dasgupta S, Sarkar U and Bumby A (2012b) The origin and maturation of lagoonal glauconites: a case study from the Oligocene Maniyara Fort Formation, western Kutch, India. *Geological Journal* **47**, 357–71.
- Banerjee S, Jeevankumar S and Eriksson PG (2008) Mg-rich ferric illite in marine transgressive and highstand systems tracts: examples from the Paleoproterozoic Semri Group, Central India. *Precambrian Research* **162**, 212–26.
- Banerjee S, Mondal S, Chakraborty PP and Meena SS (2015) Distinctive compositional characteristics and evolutionary trend of Precambrian glaucony: example from Bhalukona Formation, Chhattisgarh basin, India. *Precambrian Research* **271**, 33–48.
- Banning A, Rude TR and Dölling B (2013) Crossing redox boundaries – aquifer redox history and effects on iron mineralogy and arsenic availability. *Journal of Hazardous Materials* **262**, 905–14.
- Bansal U, Banerjee S, Pande K, Arora A and Meena SS (2017) The distinctive compositional evolution of glauconite in the Cretaceous Ukra Hill Member (Kutch basin, India) and its implications. *Marine and Petroleum Geology* **82**, 97–117.
- Bansal U, Banerjee S, Ruidas DK and Pande K (2018) Origin and geochemical characterization of Maastrichtian glauconites in the Lameta Formation, Central India. *Journal of Palaeogeography* **7**, 99–116.
- Bansal U, Pande K, Banerjee S, Nagendra R and Jagadeesan KC (2019) The timing of oceanic anoxic events in the Cretaceous succession of Cauvery basin: constraints from $^{40}\text{Ar}/^{39}\text{Ar}$ ages of glauconite in the Karai Shale formation. *Geological Journal* **54**, 308–15.
- Bau M and Dulski P (1996) Distribution of yttrium and rare-earth elements in the Penge and Kuruman Iron-Formations, Transvaal Supergroup, South Africa. *Precambrian Research* **79**, 37–55.
- Berra F, Zanchi A, Mattei M and Nawab A (2007) Late Cretaceous transgression on a Cimmerian high (Neka Valley, Eastern Alborz, Iran): a geodynamic event recorded by glauconitic sands. *Sedimentary Geology* **199**, 189–204.
- Bhattacharya B and Jha S (2014) Late Cretaceous diurnal tidal system: a study from Nimar Sandstone, Bagh Group, Narmada Valley, Central India. *Current Science* **107**, 1032–7.
- Bose PK and Das NG (1986) A Transgressive storm- and fair-weather wave dominated shelf sequence: Cretaceous Nimar Formation, Chakrud, Madhya Pradesh, India. *Sedimentary Geology* **46**, 147–67.
- Brčić V, Glumac B, Fuček L, Grizelj A, Horvat M, Posilović H and Mišur I (2017) The Cenomanian–Turonian boundary in the northwestern part of the Adriatic Carbonate Platform (Čičarija Mtn., Istria, Croatia): characteristics and implications. *Facies* **63**, 17.
- Caracciolo L, Le Pera E, Muto F and Perri F (2011) Sandstone petrology and mudstone geochemistry of the Peruc–Korycany Formation (Bohemian Cretaceous Basin, Czech Republic). *International Geology Review* **53**, 1003–31.
- Carson GA and Crowley SF (1993) The glauconite–phosphate association in hardgrounds: examples from the Cenomanian of Devon, southwest England. *Cretaceous Research* **14**, 69–89.
- Čech S, Hradecká L, Svobodová M and Švábenická L (2005) Cenomanian and Cenomanian–Turonian boundary in the southern part of the Bohemian Cretaceous Basin, Czech Republic. *Bulletin of Geosciences*, **80**, 321–54.

- Chafetz HS and Reid A** (2000) Syndepositional shallow water precipitation of glauconitic minerals. *Sedimentary Geology* **136**, 29–42.
- Chiplonkar GW and Ghare MA** (1976) Palaeontology of Bagh Beds – Part VII: Ammonoidea. *Bulletin of Earth Sciences* **4–5**, 1–10.
- Courbe C, Velde B and Meunier A** (1981) Weathering of glauconites: reversal of the glauconitization process in a soil profile in western France. *Clay Minerals* **16**, 231–43.
- Demicco RV, Lowenstein TK, Hardie LA and Spencer RJ** (2005) Model of seawater composition for the Phanerozoic. *Geology* **33**, 877–80.
- Dickson AJ, Saker-Clark M, Jenkyns HC, Bottini C, Erba E, Russo F, Gorbanenko O, Naafs BD, Pancost RD, Robinson SA and Van Den Boorn SH** (2017) A Southern Hemisphere record of global trace-metal draw-down and orbital modulation of organic-matter burial across the Cenomanian–Turonian boundary (Ocean Drilling Program Site 1138, Kerguelen Plateau). *Sedimentology* **64**, 186–203.
- El Albani A, Meunier A and Fürsich F** (2005) Unusual occurrence of glauconite in a shallow lagoonal environment (Lower Cretaceous, northern Aquitaine Basin, SW France). *Terra Nova* **17**, 537–44.
- El Kadiri K, Serrano F, Hilala R, Liemlahi H, Chalouan A, Lopez-Garrido AC, Guerra-Merch A, Sanz-De-Galdeano C, Kerzazi K and El Mrihi A** (2005) Lithostratigraphy and sedimentology of the latest Cretaceous early Burdigalian Tamezzakht succession (Northern Rif, Morocco): consequences for its sequence stratigraphic interpretation. *Facies* **50**, 477–503.
- El-Azabi MH and El-Araby A** (2007) Depositional framework and sequence stratigraphic aspects of the Coniacian–Santonian mixed siliciclastic/carbonate Matulla sediments in Nezzazat and Ekma blocks, Gulf of Suez, Egypt. *Journal of African Earth Sciences* **47**, 179–202.
- Elderfield H and Pagett R** (1986) REE in ichthyoliths: variations with redox conditions and depositional environment. *Science of the Total Environment* **49**, 175–97.
- Farouk S** (2015) Upper Cretaceous sequence stratigraphy of the Galala Plateaux, western side of the Gulf of Suez, Egypt. *Marine and Petroleum Geology* **60**, 136–58.
- Gale J, Rachmilevitch S, Reuveni J and Volokita M** (2001) The high oxygen atmosphere toward the end-Cretaceous; a possible contributing factor to the K/T boundary extinctions and to the emergence of C4 species. *Journal of Experimental Botany* **52**, 801–9.
- Gangopadhyay TK and Bardhan S** (2000) Dimorphism and a new record of Barroisiceras De Grossouvre (Ammonoidea) from the Coniacian of Bagh, Central India. *Canadian Journal of Earth Science* **37**, 1377–87.
- Gangopadhyay TK and Maiti M** (2012) Geological implication of a turreted gastropod and astartid pelecypod bearing horizon in the nodular limestone of Sukar Nala Section near Zirabad of Bagh, Dhar District, M.P., India. *Journal of Science and Technology MSU* **31**, 45–50.
- Gangopadhyay TK and Halder K** (1996) Significance of the first record of nautiloid from the Upper Cretaceous Bagh Group of rocks. *Current Science* **70**, 462–5.
- Garrison RE, Kennedy WJ and Palmer TJ** (1987) Early lithification and hardgrounds in Upper Albian and Cenomanian Calcarenes, Southwest England. *Cretaceous Research* **8**, 103–40.
- Ghabeishavi A, Moghaddam HV and Taheri A** (2009) Facies distribution and sequence stratigraphy of the Coniacian–Santonian succession of the Bangestan Palaeo-high in the Bangestan Anticline, SW Iran. *Facies* **55**, 243–57.
- Glenn CR and Arthur MA** (1990) Anatomy and origin of a Cretaceous phosphorite–greensand giant, Egypt. *Sedimentology* **37**, 123–54.
- Guinot G** (2013) Late Cretaceous elasmobranch palaeoecology in NW Europe. *Palaeogeography, Palaeoclimatology, Palaeoecology* **388**, 23–41.
- Haq BU** (2014) Cretaceous eustasy revisited. *Global and Planetary Change* **113**, 44–58.
- Harder H** (1980) Syntheses of glauconite at surface temperatures. *Clays and Clay Minerals* **28**, 217–22.
- Hardie LA** (1966) Secular variation in seawater chemistry: an explanation for the coupled secular variation in the mineralogies of marine limestones and potash evaporites over the past 600 M.Y. *Geology* **24**, 279–83.
- Harding SC, Nash BP, Petersen EU, Ekdale AA and Dyar MD** (2014) Mineralogy and geochemistry of the Main Glauconite Bed in the middle Eocene of Texas: paleoenvironmental implications for the verdine facies. *PLOS ONE* **9**, e87656. doi: 10.1371/journal.pone.0087656.
- Harris WB** (1976) Rb/Sr glauconite isochron, Maestrichtian unit of Peedee Formation (Upper Cretaceous), North Carolina. *Geology* **4**, 761–2.
- Harris WB and Bottino ML** (1974) Rb/Sr study of Cretaceous lobate glauconite pellets, North Carolina. *Geological Society of America Bulletin* **85**, 1475–8.
- Henderson RA** (1998) Eustatic and palaeoenvironmental assessment of the mid Cretaceous Bathurst Island group of the money shoals platform, northern Australia. *Palaeogeography, Palaeoclimatology, Palaeoecology* **138**, 115–38.
- Hesselbo SP and Huggett JM** (2001) Glaucony in ocean-margin sequence stratigraphy (Oligocene Pliocene, Offshore New Jersey, USA; ODP Leg 174A). *Journal of Sedimentary Research* **71**, 598–606.
- Hogg CS and Meads RE** (1970) The Mössbauer spectra of several micas and related minerals. *Mineralogical Magazine* **37**, 606–14.
- Isaac MJ, Moore PR and Joass YJ** (1991) Tahora Formation: the basal facies of a Late Cretaceous transgressive sequence, northeastern New Zealand. *New Zealand Journal of Geology and Geophysics* **34**, 227–36.
- Jaitly AK and Ajane R** (2013) Comments on *Placenticerias mintoi* (Vredenburg, 1906) from the Bagh Beds (Late Cretaceous), Central India with special reference to Turonian Nodular Limestone Horizon. *Journal of the Geological Society of India* **81**, 1–10.
- Jarrar G, Amireh B and Zachmann D** (2000) The major, trace and rare earth element geochemistry of glauconites from the early Cretaceous Kurnub Group of Jordan. *Geochemical Journal* **34**, 207–22.
- Khalifa MA** (1983) Origin and occurrence of glauconite in the green sandstone associated with unconformity, Bahariya Oases, Western Desert, Egypt. *Journal of African Earth Sciences* **1**, 321–5.
- Kotlicki A, Szczyrba J and Wiewiora A** (1981) Mössbauer study of glauconites from Poland. *Clay Minerals*, **16**, 221–30.
- Kumar S, Pathak DB, Pandey B, Jaitly AK and Gautam JP** (2018) The age of the Nodular Limestone Formation (Late Cretaceous), Narmada Basin, central India. *Journal of Earth System Science* **127**, 1–7.
- Legrand HE** (1989) An innovative hydrogeologic setting for disposal of low-level radioactive wastes. *Environmental Geology and Water Sciences* **13**, 233–9.
- Longuépée H and Cousineau PA** (2006) Constraints on the genesis of ferrian illite and aluminum-rich glauconite: potential impact on sedimentology and isotopic studies. *Canadian Mineralogist* **44**, 967–80.
- Martinec P, Vavro M, Scucka J and Maslan M** (2010) Properties and durability assessment of glauconitic sandstone: a case study on Zamel sandstone from the Bohemian Cretaceous Basin (Czech Republic). *Engineering Geology* **115**, 175–81.
- McConchic DM, Ward JB, McCann JH and Lewis DW** (1979) A Mössbauer investigation of glauconite and its geological significance. *Clays and Clay Minerals* **27**, 339–48.
- Meunier A and El Albani A** (2007) The glauconite-Fe-illite-Fe-smectite problem: a critical review. *Terra Nova* **19**, 95–104.
- Mishra UK and Sen S** (2001) Dinosaur bones from Meghalaya. *Current Science*, **80**, 1053–6.
- Núñez-Useche F, Canet C, Barragán R and Alfonso P** (2016) Bioevents and redox conditions around the Cenomanian–Turonian anoxic event in Central Mexico. *Palaeogeography, Palaeoclimatology, Palaeoecology* **449**, 205–26.
- Odin GS and Matter A** (1981) De glauconiarum origine. *Sedimentology* **28**, 611–41.
- Odin GS, Velde B and Bonhomme M** (1977) Radiogenic argon in glauconites as a function of mineral recrystallization. *Earth and Planetary Science Letters* **37**, 154–8.
- Odom EI** (1984) Glauconite and celadonite minerals. In *Micas Reviews in Mineralogy and Geochemistry*, vol. 13 (ed. SW Bailey), pp. 554–72. Washington, DC: Mineralogical Society of America.
- Olszewska-Nejbert D and Świerczewska-Gładysz E** (2013) Facies and sedimentation of Coniacian deposits of the Kraków Swell in the Wielkanoc area (southern Poland). *Geological Quarterly* **57**, 1–16.
- Ostwald J** (1990) The biogeochemical origin of the Groote Eylandt manganese oxide pisoliths and oolites, northern Australia. *Ore Geology Review* **5**, 469–90.
- Ozaki K and Tajika E** (2013) Biogeochemical effects of atmospheric oxygen concentration, phosphorus weathering, and sea-level stand on oceanic redox

- chemistry: implications for greenhouse climates. *Earth and Planetary Science Letters* **373**, 129–39.
- Parrish JT, Droser ML and Bottjer DJ** (2001) A Triassic upwelling zone: the Shublik Formation, Arctic Alaska, USA. *Journal of Sedimentary Research* **71**, 272–85.
- Parron C and Amouric M** (1990) Crystallochemical heterogeneity of glauconites and the related problem of glauconite–celadonite distinction. *Chemical Geology*, **84**, 286–9.
- Pasquini C, Lualdi A and Vercesi P** (2004) Depositional dynamics of glaucony-rich deposits in the Lower Cretaceous of the Nice Arc, Southeast France. *Cretaceous Research* **25**, 179–89.
- Prélat A, Hodgson DM, Hall M, Jackson CAL, Baunack C and Tveiten B** (2015) Constraining sub-seismic deep-water stratal elements with electrofacies analysis: a case study from the Upper Cretaceous of the Måloy Slope, offshore Norway. *Marine and Petroleum Geology* **59**, 268–85.
- Rea DK, Dehn J, Driscoll NW, Farrell JW, Janecek TR, Pospichal RJJ and Resiwati P** (1990) Paleooceanography of the eastern Indian Ocean from ODP Leg 121 drilling on Broken Ridge. *Bulletin of the Geological Society of America* **102**, 679–90.
- Retzler A, Wilson MA and Avni Y** (2013) Chondrichthyans from the Menuha Formation (Late Cretaceous: Santonian Early Campanian) of the Makhtesh Ramon region, southern Israel. *Cretaceous Research* **40**, 81–9.
- Rifai IR and Shaaban MN** (2007) Authigenic dolomite cementation in the Upper Cretaceous Phosphate Formation, Western Desert, Egypt. *Sedimentary Geology* **202**, 702–9.
- Robert M** (1973) The experimental transformation of mica toward smectite; relative importance of total charge and tetrahedral substitution. *Clays and Clay Minerals* **21**, 167–74.
- Rolf RM, Kimball CW and Odom IE** (1977) Mössbauer characteristics of Cambrian glauconite, central U.S.A. *Clays and Clay Minerals* **25**, 131–7.
- Rousset D, Leclerc S, Clauer N, Lancelot J, Cathelineau M and Aranyosy JF** (2004) Age and origin of Albian glauconites and associated clay minerals inferred from a detailed geochemical analysis. *Journal of Sedimentary Research* **74**, 631–42.
- Ruidas DK, Paul S and Gangopadhyay TK** (2018) A reappraisal of stratigraphy of Bagh Group of rocks in Dhar District, Madhya Pradesh with an outline of origin of nodularity of Nodular Limestone Formation. *Journal of the Geological Society of India* **92**, 19–26.
- Salamon MA** (2007) First record of bourgueticrinid crinoids from the Cenomanian of southern Poland. *Cretaceous Research* **28**, 495–9.
- Schwimmer DR, Padian K and Woodhead AB** (1985) First Pterosaur records from Georgia: open marine facies, Eutaw Formation (Santonian). *Journal of Paleontology* **59**, 674–6.
- Selby D** (2009) U/Pb zircon geochronology of the Aptian/Albian boundary implies that the GL–O international glauconite standard is anomalously young. *Cretaceous Research* **30**, 1263–7.
- Sharafi M, Mahboubi A, Moussavi-Harami R, Ashuri M and Rahimi B** (2013) Sequence stratigraphic significance of sedimentary cycles and shell concentrations in the Aitamir Formation (Albian–Cenomanian), Kopet–Dagh Basin, northeastern Iran. *Journal of Asian Earth Sciences* **67–68**, 171–86.
- Stephenson LW** (1929) Unconformities in the Upper Cretaceous series of Texas. *AAPG Bulletin* **13**, 323–34.
- Tandon SK** (2000) Spatio-temporal patterns of environmental changes in Late Cretaceous sequences of Central India. In *Cretaceous Environments of Asia* (eds H Okada and NJ Mateer) pp. 225–41. Developments in Palaeontology and Stratigraphy, vol. 17. Amsterdam: Elsevier.
- Tang D, Shi X, Ma J, Jiang G, Zhou X and Shi Q** (2017) Formation of shallow-water glaucony in weakly oxygenated Precambrian ocean: an example from the Mesoproterozoic Tieling Formation in North China. *Precambrian Research* **294**, 214–29.
- Tewari VC, Lokho K, Kumar K and Siddaiah NS** (2010) Late Cretaceous Paleogene basin architecture and evolution of the Shillong shelf sedimentation, Meghalaya, northeast India. *Journal of the Indian Geological Congress* **2**, 61–73.
- Thompson GR and Hower J** (1975) The mineralogy of glauconite. *Clays and Clay Minerals* **23**, 289–300.
- Timofeeff MN, Lowenstein TK, Da Silva MAM and Harris NB** (2006) Secular variation in the major-ion chemistry of seawater: evidence from fluid inclusions in Cretaceous halites. *Geochimica et Cosmochimica Acta* **70**, 1977–94.
- Varol B, Özgüner AM, Koşun E, Imamğolu Ş, Daniş M and Karakullukçu T** (2000) Depositional environments and sequence stratigraphy of glauconites of western Black Sea region. *Mineral Research and Exploration Bulletin* **122**, 1–21.
- Walker RG and Bergman KM** (1993) Shannon Sandstone in Wyoming: a shelf-ridge complex reinterpreted as lowstand shoreface deposits. *Journal of Sedimentary Research* **63**, 839–51.
- Westermann S, Caron M, Fiet N, Fleitmann D, Matera V, Adatte T and Föllmi KB** (2010) Evidence for oxic conditions during oceanic anoxic event 2 in the northern Tethyan pelagic realm. *Cretaceous Research* **31**, 500–14.
- Wilmsen M, Niebuhr B and Hiss M** (2005) The Cenomanian of northern Germany: facies analysis of a transgressive biosedimentary system. *Facies* **51**, 242–63.
- Witts JD, Bowman VC, Wignall PB, Crame JA, Francis JE and Newton RJ** (2015) Evolution and extinction of Maastrichtian (Late Cretaceous) cephalopods from the López de Bertodano Formation, Seymour Island, Antarctica. *Palaeogeography, Palaeoclimatology, Palaeoecology* **418**, 193–212.
- Wright J, Schrader H and Holser W** (1987) Paleoredox variations in ancient oceans recorded by rare earth elements in fossil apatite. *Geochimica et Cosmochimica Acta* **51**, 631–44.
- Yilmaz IO, Altiner D, Tekin UK and Ocakoglu F** (2012) The first record of the “mid-Barremian” Oceanic Anoxic Event and the late Hauterivian platform drowning of the Bilecik platform, Sakarya Zone, western Turkey. *Cretaceous Research* **38**, 16–39.
- Yilmaz IO, Cook TD, Hosgor I, Wagreich M, Rebman K and Murray AM** (2018) The upper Coniacian to upper Santonian drowned Arabian carbonate platform, the Mardin-Mazidag area, SE Turkey: sedimentological, stratigraphic, and ichthyofaunal records. *Cretaceous Research* **84**, 153–67.
- Zalat AA, Zaid SM, Gadallah MH and Abdel-Aziz ZA** (2012) Sandstones reservoir quality of the Matulla Formation, Gulf of Suez, Egypt. *Australian Journal of Basic and Applied Sciences* **6**, 511–29.
- Žítt J, Vodrážka R, Hradecká L, Svobodová M, Štátný M and Švábenická L** (2015) Depositional and palaeoenvironmental variation of lower Turonian nearshore facies in the Bohemian Cretaceous Basin, Czech Republic. *Cretaceous Research* **56**, 293–315.